Supplementary Information for

Surface-Functionalized Boron Nanosheets and their Suprastructures with Unprecedented Proton-Transport Properties

Hongfeng Zhan[1,2], Mengwei Dong[2], Shengchuang Qiu[1], Xiaoshan Wang[3], Lingfeng Chao[3], Zhendong Huang[1], Yonghua Chen[2,3], Hai Li[2], Xiao Huang,[2,3], Shaozhou Li[1*]*

1 State Key Laboratory of Organic Electronics and Information Displays & Institute of Advanced Materials, Nanjing University of Posts & Telecommunications, 9 Wenyuan Road, Nanjing 210023, China

2 Key Laboratory of Flexible Electronics (KLOFE) & Institute of Advanced Materials (IAM), Jiangsu National Synergistic Innovation Center for Advanced Materials (SICAM), Nanjing Tech University (NanjingTech), 30 South Puzhu Road, Nanjing 211816, China

3 Shaanxi Institute of Flexible Electronics (SIFE), Northwestern Polytechnical University (NPU), 127 West Youyi Road, Xi'an 710072, Shaanxi, China.

Methods

Synthesis of B-CH_3 particles

In a typical synthesis of B-CH_3, 0.5 g MgB_2 powder (>99%, Sigma-Aldrich), 3g iodine beads (>99%, Aladdin Chemical Reagent Co. Ltd) were mixed with 50 ml methanol ((>99.8%, ACS grade, Aladdin Chemical Reagent Co. Ltd) and stirred for 5 min to dissolve the iodine beads. The mixture was then cooled by ice bath for 1 h before 0.5 mL 4M HCl (Technical reagent, Nanjing Chemical Reagent Co. Ltd) was dropwise added. The mixture was stirred for one week at room temperature. The product was washed with methanol four times and ultrasonic to yield isolated methyl-functionalized boron nanosheets.

Synthesis of boron nanosheet suprastructures

In a typical synthesis, 50 mg B-CH_3 particles was placed in 15 mL plastic tube. 10 mL DI water was added. For the synthesis of microspherical suprastructures, the mixture was shaken and fast freeze by liquid N_2 before lyophilized in a vacuum freeze drier for 24 h. For the synthesis of wire-like suprastructures, the mixture was centrifuged to remove the bubbles before fast freeze by liquid N_2. The product was dried using a vacuum oven at 60^{o}C.

Materials characterizations

X-ray diffraction (XRD, Bruker D8) was performed with Cu Kα radiation (λ = 1.54 Å) as the X-ray source. The UV-vis-NIR absorption spectrum was record by LAMBDA 650S. Scanning electron microscopy (SEM, Hitachi S-4800) was used for the morphology analysis. To gain the crystal structure information, high-resolution transmission electron microscopy (HRTEM, JEOL 2100F) coupled with energy dispersive X-ray (EDX) spectroscopy analyses were performed. The chemical state study of the samples was carried out by X-ray photoelectron spectroscopy (XPS, PHI 5000 VersaProbe) and the binding energies were corrected for specimen charging effects using the C 1s level at 284.6 eV as the reference. The lineshapes used for XPS curve fitting were Lorentzian-Gaussian (L/G=80%) and integrated backgrounds were employed. The Auger electron spectra were obtained from Kratos Axis Supra X-ray photoelectron spectrometer with Auger analysis. X-ray total scattering data used to generate PDFs were collected using Bruker D8 Quest with Mo source and PDFs were simulated using the PDFgui program. Thermogravimetric analysis (TGA, NETZSCH STA409) was conducted with a heating/cooling rate of 10 ℃ min^{-1} between 30 to 700 ^{o}C under N_2 atmosphere.

Electrochemical Measurements

The pellets were compressed in a homemade device, and both sides of the pellets were attached to the copper electrode. The impedance measurements were carried out by using an Autolab electrochemical workstation (Autolab 302N) with tunable frequency ranging from 10 Hz to 1 MHz and an alternating potential of 100 mV. Conductivities at different temperatures were tested in a constant temperature & humidity chamber.

The product powder of 1 mg were dispersed in 1 mL ethanol. The mixtures were then drop-coated on the SiO_2/Si substrates with pre-patterned Cr/Au electrode deposited through evaporating deposition. Current at the applied voltage of 1 V was measured by a source measurement unit system (Keithley 4200) at room temperature. Properties of the humidity sensor were performed by exposing it to water vapors with different RH values, which were realized by several specified saturated salt solutions to obtain the corresponding supersaturation aqueous solutions in a closed vessel. We use saturated LiCl, $MgCl_2$, NaBr, NaCl and K_2SO_4 solutions which can provide approximately 11%, 33%, 55%, 75%, and 97% RH, respectively.

DFT simulation of the nanosheet

DFT calculations were performed using the plane-wave technique realized in the CASTEP program.[38] The electron-ion interactions were described by the projector augmented plane wave (PAW) pseudopotentials. Perdew-Burke-Ernzerhof (PBE) functional was used to express the generalized gradient approximation (GGA). A cut off energy of 520 eV and the total energy converged to less than 10^{-6} eV per atom were used for optimization criteria and the maximum force was converged to lower than 0.02 eV/Å for all the 2D monolayer boron nanosheet. The atomic structure for simulation is directly derived from the fitted local structure of the boron nanosheet based on XPDF fitting and the geometric optimization was carried out before further simulation.

For the calculation of the activation barriers for proton diffusion through the nanosheet, the reaction systems were modelled by optimizing a proton above and below a single nanosheet. The simulations were carried out in a 3×3 supercell, extended infinitively in the x and y dimensions. A 15 Å gap was inserted between the graphene layer perpendicular to the surface. The penetration route is considered with both ends fixed 3 Å above the mid of the pores formed by the boron nanosheet first, then relaxed to the most stable proton adsorption sites on the 2D structures. The nudged elastic band method was used to provide an initial transition state structure that was used in the subsequent dimer simulations to isolate the transition state. The

reaction barrier was defined as the energy difference between the transition state and the reaction state minimum.

Measurements of electronic conduction contribution

To identify the possible electronic conduction contribution to the conductivity of boron nanosheets, Pt electron blocking electrodes were used to measure the ionic transference number (t_{ion}) of the membranes by Wagner's polarization technique.[1] Here Pt works as the blocking electrodes. The pressed memberane is coated with Pt on both sides to form a Pt//boron nanosheets//Pt sandwiched pellet structure. The pellet is placed in a homemade device (Fig. SX) for chronoamperometry measurement. Current passing through the membranes was monitored in a 2-probe configuration using Pt electrodes attached on the surface of membranes under a constant voltage (1 V). Through Wagner's polarization technique, the contribution of ions to the current is diminished with time due to the blocking effect of Pt. Under steady-state conditions, migration of ions due to the electrical field is balanced by diffusion due to the concentration gradient, and the current is carried exclusively by electrons moving. The current decreases to almost zero at steady state, meaning the boron nanosheet is electron insulator. Therefore, the initial current measured by chronoamperometry is attributed to proton conduction. All the measurements were carried out at 0% RH atmosphere to eliminate the ion conductivity. t_{ion} was calculated as follows:

$$t_{ion} = \frac{i_t - i_e}{i_t}$$

where i_t is the total current, and i_e is the electronic current. The calculated transference number is 0.996, proving the dominate contribution of proton conduction to the current.

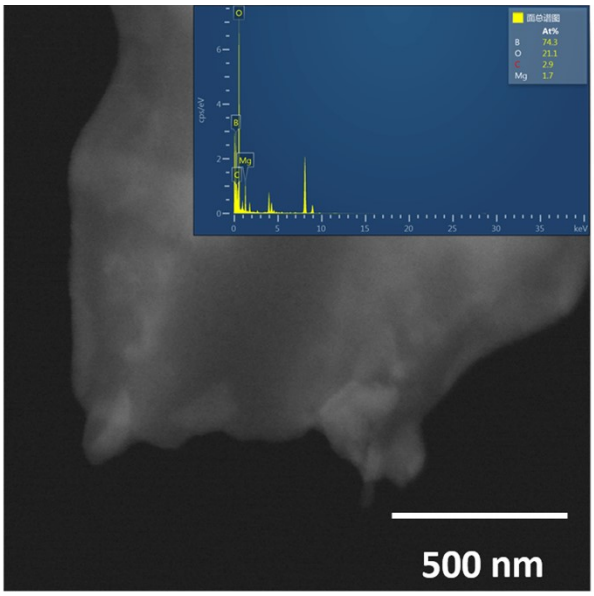

Supplementary Figure 1. STM image and EDS of the B-B boron nanosheets.

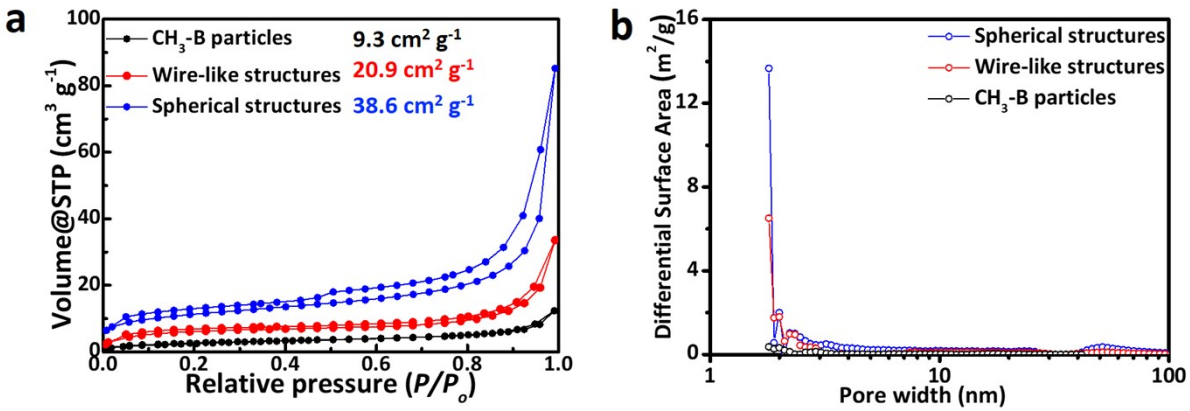

Supplementary Figure 2. a, The N_2 isotherms of CH_3-B, microwire and microsphere of the boron nanosheets. **b**, Their pore size distributions calculated based on non-local density functional theory (NLDFT) model. It shows the presence of micropores (~1 nm) in the bifunctionalized boron nanosheet which may relate to the formation of B vacancy surface.

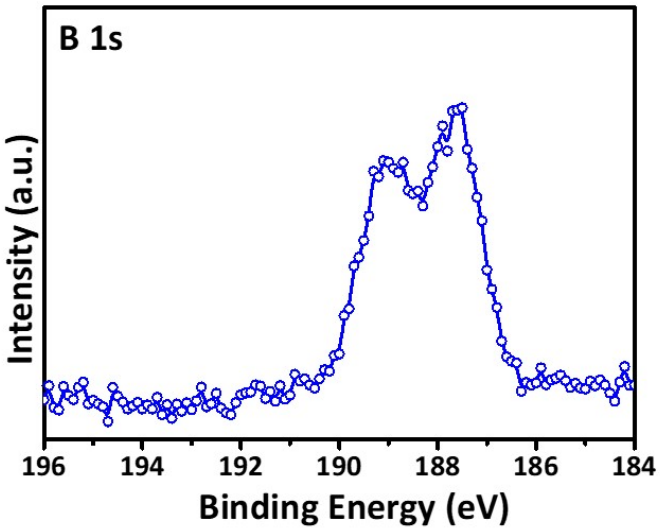

Supplementary Figure 3. High-resolution B1s spectra of the B-B nanosheets after exposure in air for six months.

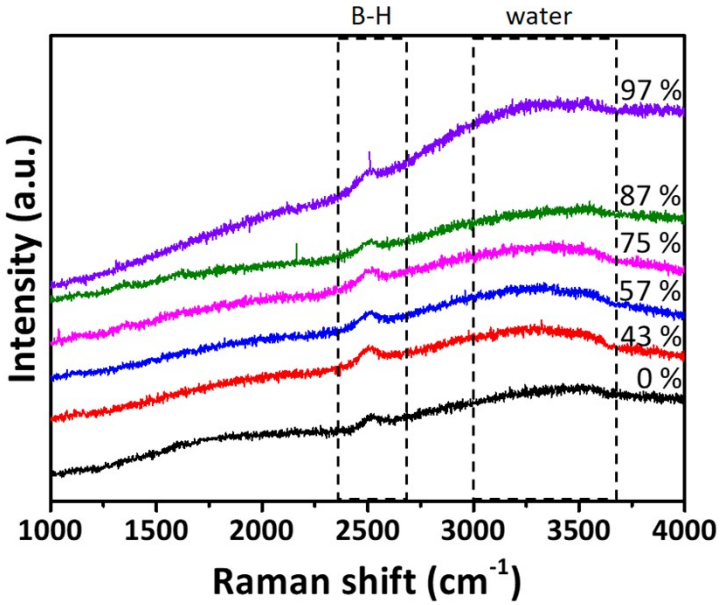

Supplementary Figure 4. Raman spectra of B-B nanosheets at different RH. The peak from 3000 to 3750 cm^{-1} is assigned to the adsorbed water, proving the structure is highly hydrophilic. The peak position at ~2500 cm^{-1} can be assigned to the B-H stretching mode. The low intensity of such peak implies the boron nanosheet is defective.

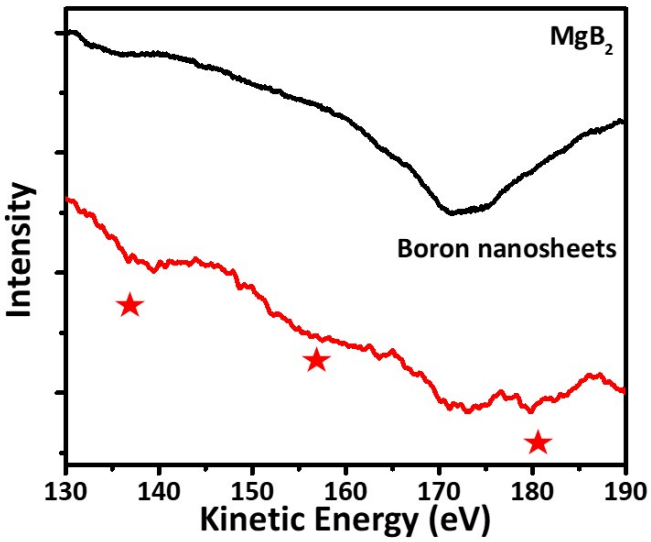

Supplementary Figure 5. Auger spectra of B for MgB_2 and the B-B nanosheets, where the red stars stand for the peaks attributed to the B spectrum in sp^3 hybridization states. The preservation of the characteristic peak (~172 eV) assigned to the sp^2 state of B implies a retained ring-like B structures in the boron nanosheets inherited from MgB_2. However, the appearance of sp^3 peaks suggest that the pristine planar B structure seems buckled.
The low intensity of such peak implies the boron nanosheet is defective.

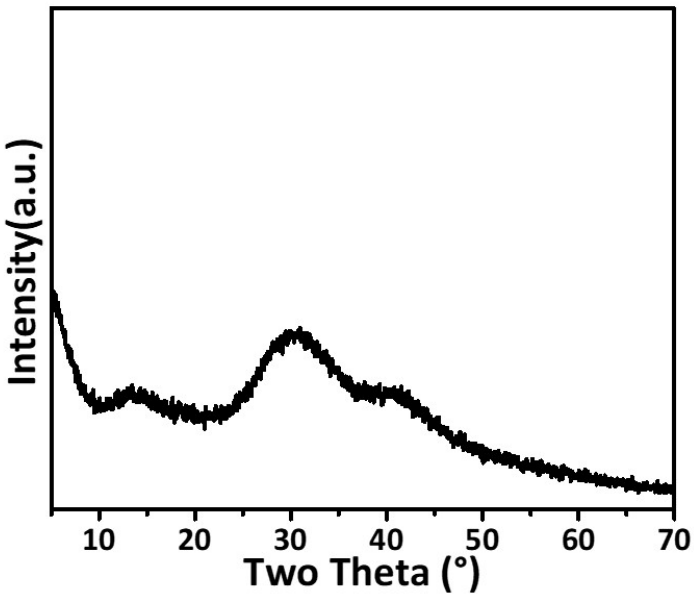

Supplementary Figure 6. XRD pattern of the B-B nanosheets after annealing in Ar gas at 600°C for half a hour. Compared to the prestine B-B nanosheets, it clearly shows that two broad peaks at ~30° and 40° are formed, indicating the enhanced atomic order of the product after annealing.

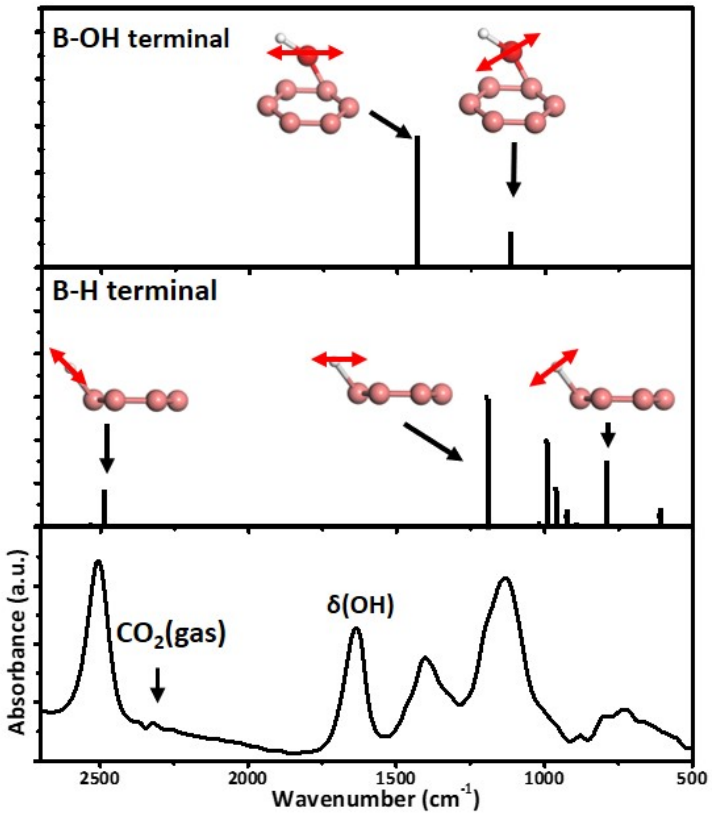

Supplementary Figure 7. The FTIR spectrum analysis and calculations. The calculated B-OH and B-H vibrations in B_6 networks are shown on the top and the FTIR spectrum of bifunctionalized B-B nanosheets is shown on the bottom. The postion of the IR peaks are matched to the calculated results.

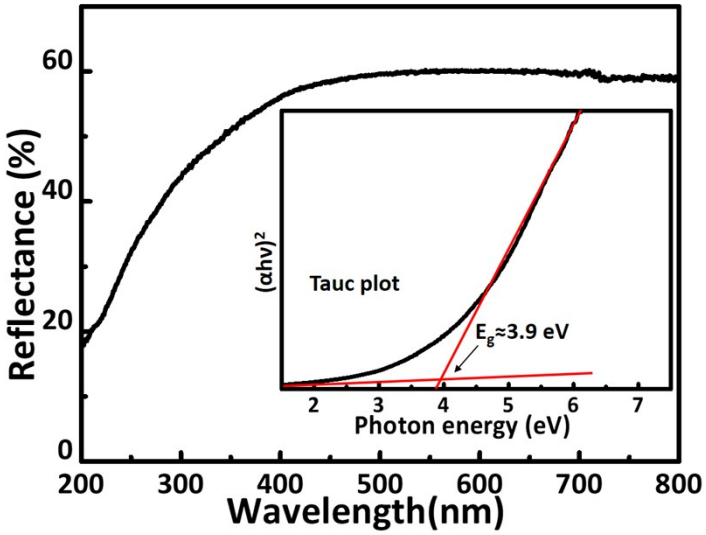

Supplementary Figure 8. UV-Vis reflective spectrum of the boron nanosheets, the bandgap energy of the boron sheet is estimated to be 3.9 eV according to the optical absorption.

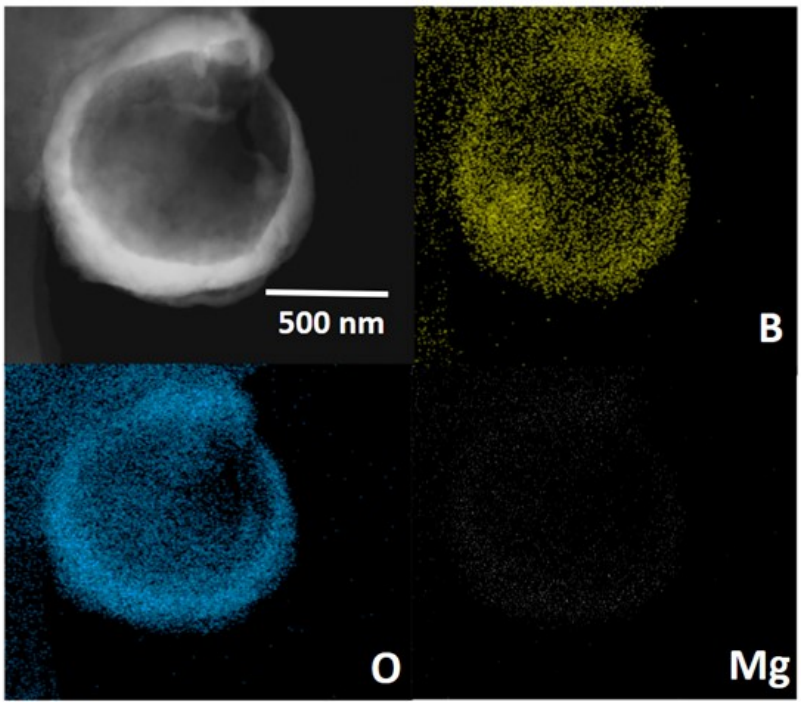

Supplementary Figure 9. Elemental mapping of the micro-spherical boron suprastructure.

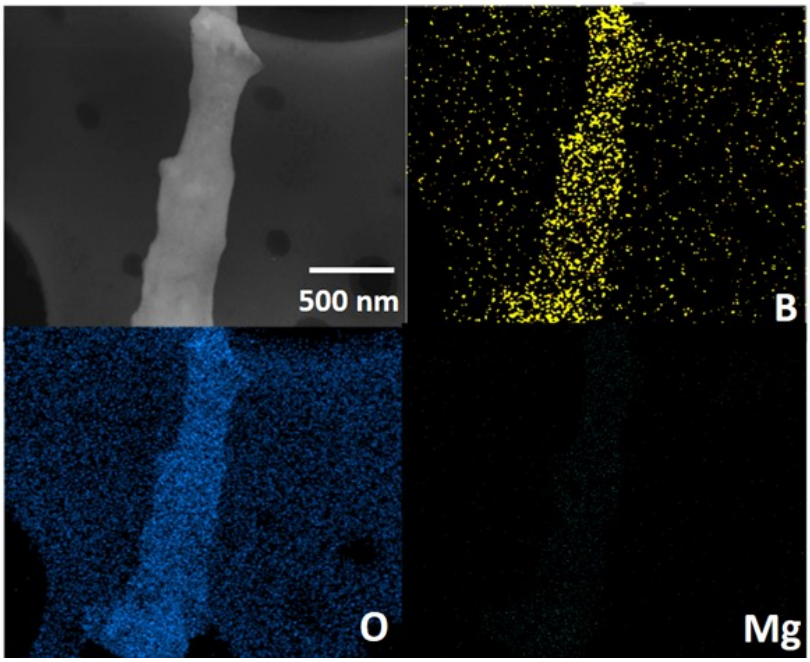

Supplementary Figure 10. Elemental mapping of the boron nanosheet micro-wire.

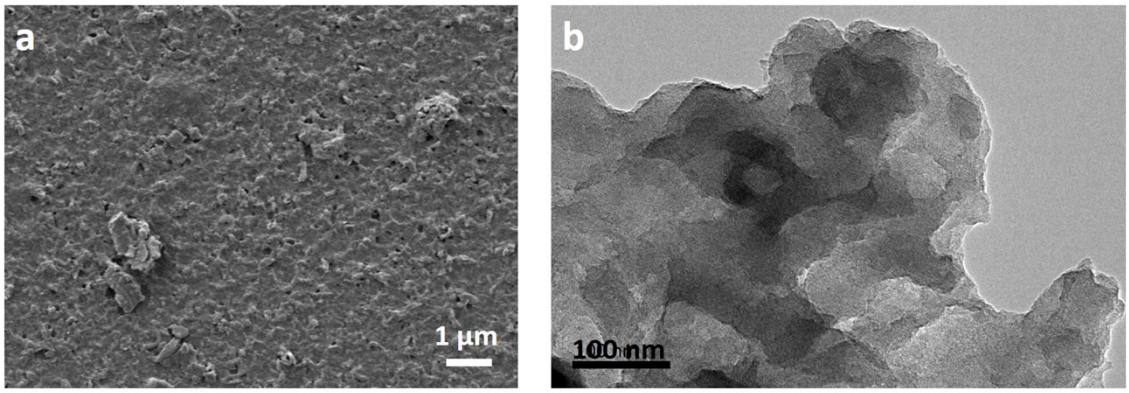

Supplementary Figure 11. **a**, SEM and **b**, TEM images of the boron nanosheet micro-wire dispersed and sonicated in methnol solution. The assembled suprastructure is disassembled and nanosheets random stacked on the substrate are observed.

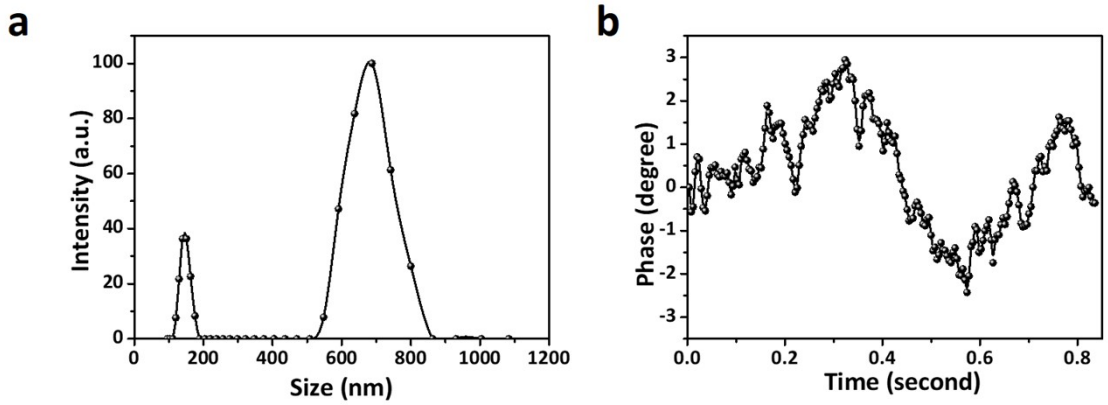

Supplementary Figure 12. a, Dynamic light scattering (DLS) result of the micro-spherical boron suprastructures in water. **b**, Zeta potential measurement of the micro-spherical boron suprastructures in water. It shows a positive charge (5.7 mV) for the hydrodynamic nanosheets.

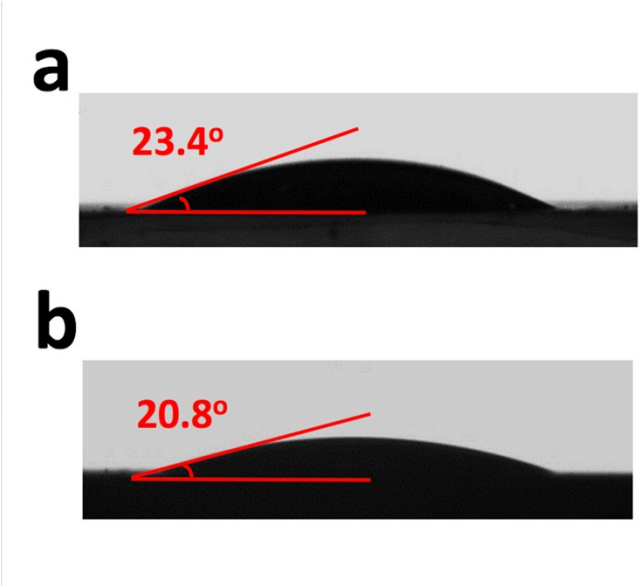

Supplementary Figure 13. Wettability of **a**, microwire boron nanosheet suprastructure and **b**, microsphere boron nanosheet suprastructure towards water.

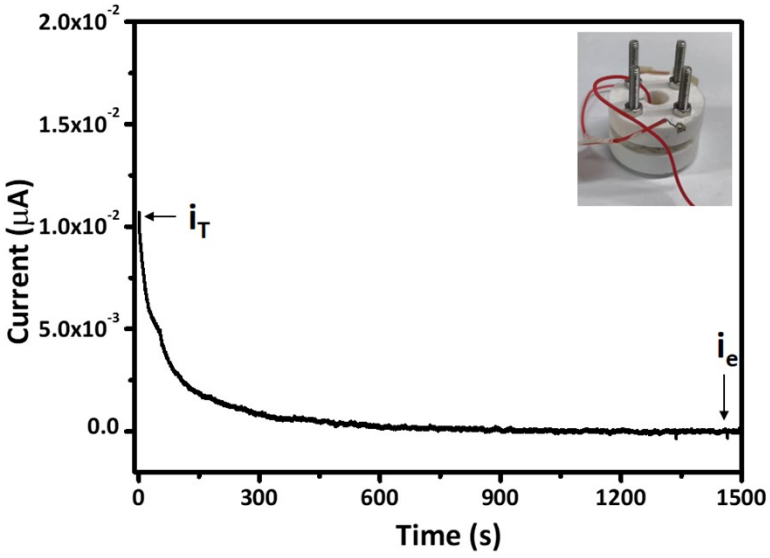

Supplementary Figure 14. Polarization plot measured by chronomaperometry (V=1 V) for the boron nanosheet membrane at 25 °C. The contribution of proton conduction to the conductivity of boron nanosheets was calculated ~0.996. Inset is the custom-made measurement device.

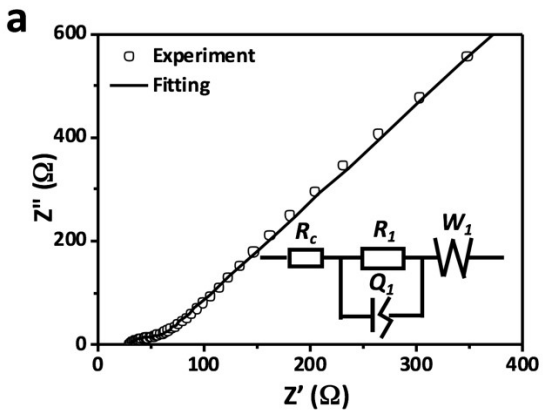

b

Element	Parameter	Value
R_1	R/Ω	24.1
Q_1	Y_0	$1.13X10^{-6}$
	N	0.886
W_1	Y_0	$49.1X10^{-6}$
	N	0.689

Supplementary Figure 15. a, Nyquist plot of impedance for the boron nanosheet membrane at 30 °C and 100% RH. The plot typically contains a semicircle at high frequencies which represents the proton impedance and an incline spur at low frequencies which represents the pile up of protons at the electrodes. The inset is the diagram of the equivalent circuit used to analyze the impedance data. R_1 and Q_1 correspond to the inner protonic transport resistance and the dielectric capacitance between the membrane and electrode, respectively. **b**, Table of the fitting data for each element in the equivalent circuit.

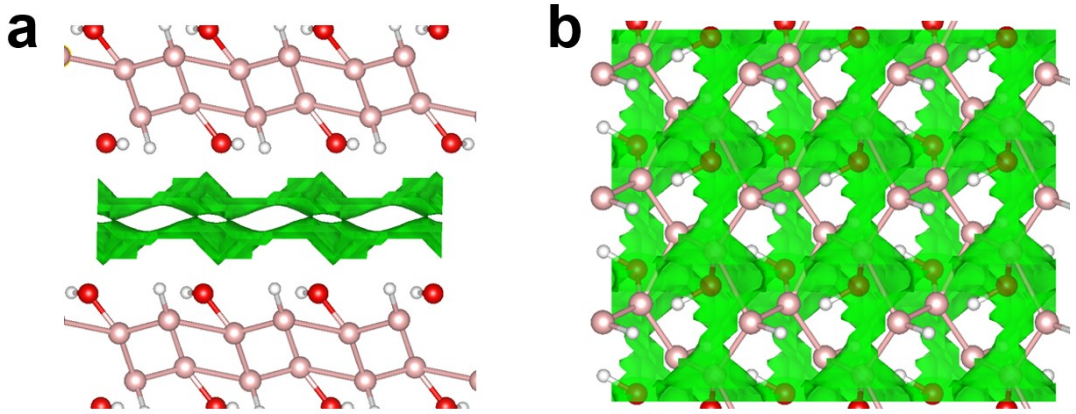

Supplementary Figure 16. Proton diffusion pathways in the 2D boron nanosheets view along different directions.

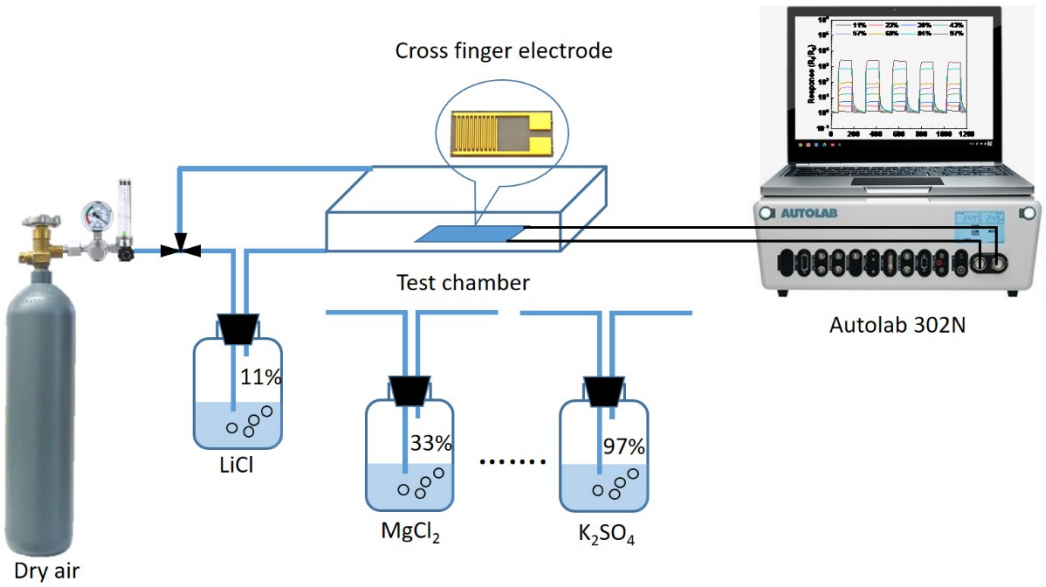

Supplementary Figure 17. Schematic diagram of the humidity sensing measurement system.

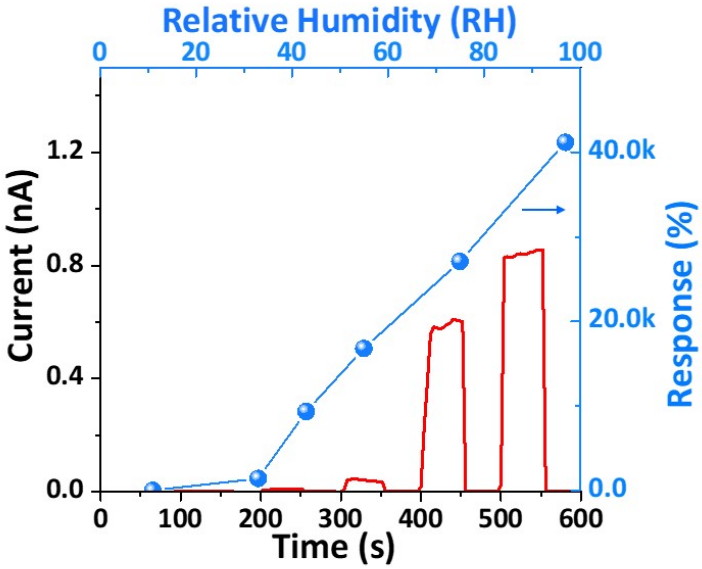

Supplementary Figure 18. Humidity sensing behaviors of the boron nanosheet sensor under switching RH.

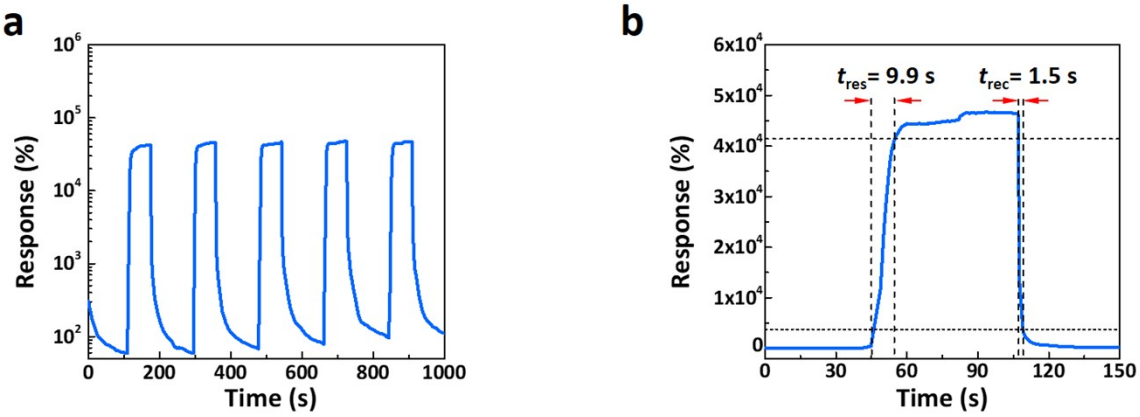

Supplementary Figure 19. a, Typical repeatability test of the boron nanosheet sensor at 97% RH. **b**, Response and recovery curve of the boron nanosheet sensor at 97% RH.

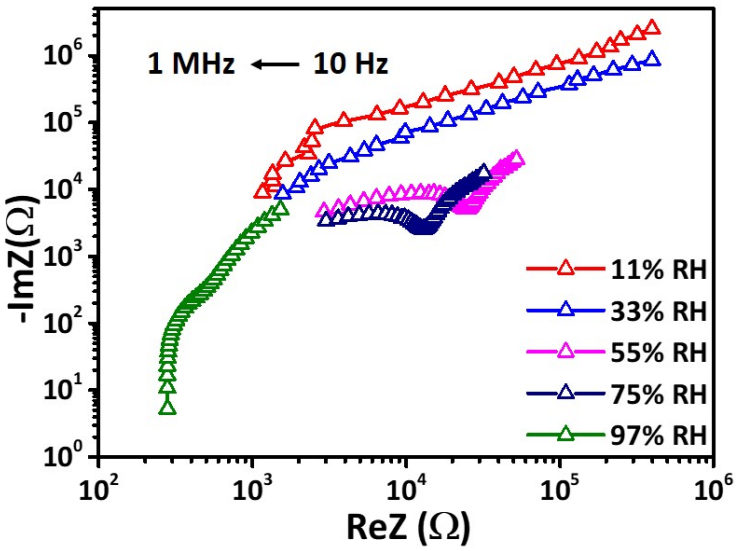

Supplementary Figure 20. Complex impedance plots of the boron nanosheet humidity sensor measured at 11%, 33%, 55%, 75%, and 97% RH with the sweeping frequency from 10 Hz to 1M Hz.

Table S1. Proton transport properties of various two-dimensional materials

Material	T (°C)	RH (%)	Conductivity (mS cm^{-1})	Ref.
$Co-Al-CO_3^{2-}$ LDH	60	80%	~0.1	[2]
$Co-Al-NO_3^{-}$ LDH	60	80%	~4	[2]
$Co-Ni-Br^{-}$ LDH	60	80%	~0.5	[2]
$Mg-Al-CO_3^{2-}$ LI	25	80%	~0.1	[3]
$Ni-Al-CO_3^{2-}$ LD	80	80%	13	[4]
Titanium oxide nanosheet	25	90%	3.04	[5]
GO	87	95%	15	[6]
Ozonated GO	25	100%	2.25	[7]
Sulfonated GO	30	100%	15	[8]
Oxygen functionalized few-layer graphene	80	95%	8.7	[9]
$(NH_4)_2(adp)[Zn_2(ox)_3]\cdot 3H_2O$	25	98%	8	[10]
$Zn_2(SO_3)_2(C_6N_3O_2H_9)_2\cdot H_2O$	75	98%	~1	[11]
$(enH_2)_4Na_2[V_{12}B_{18}O_{54}(OH)_6(H_2O)]\cdot 7H_2O$	60	100%	0.2	[12]
Imidazole linked-2D-polymer	95	95%	32	[13]
KAUST-7’	90	95%	20	[14]

Table S2. Humidity sensing of various two-dimensional materials.

Material	Response(%)	Humidity range	Response(s)/ recovery (s)	Applied Voltage (V)	Sensing Principle	Reference
$NiPS_3$	10^6	0 - 10%	<3/3	4	resistance	[15]
$SnSe_2$ /MWCNT	857	10 - 95%	1.8/2.9	-1-1	resistance	[16]
$SnSe_2$ nanosheets	483	10 - 95%	3.8/3.9	-1-1	resistance	[16]
Lead free $Cs_2BiAgBr_6$	1162	15 - 78%	1.78/0.45	0-10	resistance	[17]
GO	120000	40 - 88%	5/6	0.5	capacitance	[18]
BP	507825	11 - 97%	4.7/3.0	0.5	capacitance	[18]
VS_2	30	0–100%	30–40/12–50	1	resistance	[19]
WS_2	3750	40–80%	13/17	1	resistance	[20]
Au/g-C_3N_4	10^5	11 - 95%	46.4/42.8	1	impedance	[21]
$TiSi_2$	3990.90	0 - 100%	0.9/8	1	impedance	[22]
BP	10^4	10 - 85%	<5	0.5	resistance	[23]
$Ti_3C_2T_x$ MXene	200-250	11-95%	1/201		resistance	[24]

Data of the fitted 2D boron nanosheet

data_BHBOH
_symmetry_cell_setting monoclinic
_symmetry_space_group_name_H-M 'P 21'
_symmetry_Int_Tables_number 1
loop_
_symmetry_equiv_pos_site_id
_symmetry_equiv_pos_as_xyz
1 x,y,z
2 -x,1/2+y,-z
_cell_length_a 7.631919
_cell_length_b 3.957492
_cell_length_c 3.320741
_cell_angle_alpha 90.00000
_cell_angle_beta 88.84081
_cell_angle_gamma 90.00000
loop_
_atom_site_label
_atom_site_type_symbol
_atom_site_fract_x
_atom_site_fract_y
_atom_site_fract_z

H H1 0.281584 -0.05503 0.210390
H H2 0.733005 0.141562 0.555332
O O1 0.284970 0.168543 1.064341
B B1 0.435489 0.195817 0.788795
B B2 0.384806 0.439908 0.359160

Reference:

[1] Xitang Qian, Long Chen, Lichang Yin, Zhibo Liu, Songfeng Pei, Fan Li, Guangjin Hou, Shuangming Chen, Li Song, Khalid Hussain Thebo, Huiming Cheng, Wencai Ren. $CdPS_3$ nanosheets-based membrane with high proton conductivity enabled by Cd vacancies. Science 2020, 370, 596-600.

[2] Pengzhan Sun, Renzhi Ma, Takayoshi Sasaki. Recent progress on exploring exceptionally high and anisotropic H^+/OH^- ion conduction in two-dimensional materials. Chem. Sci., 2018, 9, 33-43.

[3] Daijun Kubo, Kiyoharu Tadanaga, et al. Hydroxide ion conduction mechanism in Mg-Al CO_3^{2-} layered double hydroxide J. Electrochem. Sci & Tech., 2021, 12, 230-236.

[4] Daiju Kubo, Kiyoharu Tadanaga, et al. Hydroxide ion conductioin in Ni-Al layered double hydroxide. J. Electroanaly. Chem. 2012, 671, 102-105.

[5] Hiroki Yasutake, Saidul Islam, et al. High proton conductivity from titanium oxide nanosheets and their variation based on crystal phase. Bull. Chem. Soc. Jpn., 2021, 94, 1840-1845.

[6] Mohammad Razaul Karim, Kazuto Hatakeyama, et al. Graphene oxide nanosheet with high proton conductivity. J. Am. Chem. Soc. 2013, 135, 8097-8100.

[7] Wei Gao, Gang Wu. et al. Ozonated graphene oxide film as a proton-exchange membrane. Angew. Chem. Int. Ed. 2014, 53, 3588–3593.

[8] K. Ravikumar, K. Scott, Freestanding sulfonated graphene oxide paper: A new polymer electrolyte for polymer electrolyte fuel cells. Chem. Commun. 2012, 48, 5584-5586.

[9] Chanderpratap Singh, Nikhil S.; et al. Proton conduction through oxygen functionalized few-layer graphene. Chem. Commun., 2016, 52, 12661-12664.

[10] Satoshi Miyatsu, Maiko Kofu, et al. Proton dynamics of two-dimensional oxalate-bridge coordination polymers. Phys. Chem. Chem. Phys., 2014, 16, 17295-17304.

[11] Yike Ma, Liangliang Huang, et al. High proton conductivity behavior in a 2D metal sulfite constructured from a histidine ligand. RCS Adv. 2019, 9, 16130-16135.

[12] Le Zhang, Xinxin Liu, et al. Facile proton conduction in a new 2D layered vanadoborate. J. Alloy & Compounds 2018, 743, 136-140.

[13] Kayaramkodath C Ranjeesh, Rajith Illathvalappil, et al. Imidazole-linked crystalline two-dimensional polymer with ultrahigh proton-conductivity. J. Amer. Chem. Soc., 2019, 141, 14950-14954.

[14] Paulo G. M. Mileo, Karim Adil, et al. Achieving superprotonic conduction with a 2D fluorinated metal-organic framework. J. Am. Chem. Soc., 2018, 140, 13156-13160.

[15] Ramesh Naidu Jenjeti, Rajat Kumar, et al. Two-dimensional, few-layer $NiPS_3$ for flexible humidity sensor with high selectivity. J. Mater. Chem. A., 2019, 7, 14545-14551

[16] Mohit Tannarana, Pratik M. Pataniya, et al. Humidity Sensor Based on Two-Dimensional $SnSe_2$/MWCNT Nanohybrids for the Online Monitoring of Human Respiration and a Touchless Positioning Interface. ACS Sustainable Chem. Eng., 2020, 8, 33, 12595–12602.

[17] Zhenhua Weng, Jiajun Qin, et al. Lead-Free $Cs_2BiAgBr_6$ Double Perovskite-Based

Humidity Sensor with Superfast Recovery Time. Adv. Funct. Mater., 2019, 29, 1902234.
[18] Pei He, Jack Brent, et al. Fully printed high performance humidity sensors based on two-dimensional materials. Nanoscale, 2018, 10, 5599.
[19] Jun Feng, Lele Peng et al. Giant Moisture Responsiveness of VS_2 Ultrathin Nanosheets for Novel Touchless Positioning Interface. Adv. Mater., 2012, 24, 1969–1974.
[20] Ravindra Kumar Jha and Prasanta Kumar Guha. Liquid exfoliated pristine WS_2 nanosheets for ultrasensitive and highly stable chemiresistive humidity sensors. Nanotechnology, 2016, 27, 475503.
[21] Shuguo Yu, Hongyan Zhang, et al. Preparation and mechanism investigation of highly sensitive humidity sensor based on two-dimensional porous Gold/Graphite carbon nitride nanoflake. Sensor. Actuat. B-chem., 2020, 307, 127679.
[22] Rayyan Ali Shaukat, Muhammad Umair Khan, et al. All range highly linear and sensitive humidity sensor based on 2D material $TiSi_2$ for real-time monitoring. Sensor. Actuat. B-chem., 2021, 345, 130371.
[23] Poya Yasaei, Amirhossein Behranginia, et al. Stable and Selective Humidity Sensing Using Stacked Black Phosphorus Flakes. ACS Nano., 2015, 9, 10, 9898–9905.
[24] Zijie Yang, Ao Liu, et al. Improvement of Gas and Humidity Sensing Properties of Organ-like MXene by Alkaline Treatment. ACS Sens., 2019, 4, 1261−1269.